ACS APPLIED MATERIALS & INTERFACES

Research Article

www.acsami.org

Incorporation of MnO_2-Coated Carbon Nanotubes between Graphene Sheets as Supercapacitor Electrode

Zhibin Lei, Fuhua Shi, and Li Lu*

Department of Mechanical Engineering, National University of Singapore, 9 Engineering Drive 1, 117576, Singapore

Supporting Information

ABSTRACT: Hierarchical graphene-based composite consisting of graphene sheets intercalated by MnO_2-coated carbon nanotubes (MnC) was prepared for high-performance supercapacitor electrode. The highly negatively charged graphene oxides reduced by urea (RGO) and the positively charged MnC functionalized with poly(diallyldimethylammonium chloride) created a strong electrostatic interaction, forming a hierarchical nanostructure. The elelctrocapacitive behaviors of MnC/RGO (MnC-G) were systematically investigated by cyclic voltammetry, galvanostatic charge−discharge and electrochemical impedance spectroscopy. A maximum specific capacitance of 193 F/g was achieved for the MnC-G composite with 37% RGO, which was almost 3-fold higher than 69 F/g of carbon nanotubes/RGO and 2-fold higher than 89 F/g of MnO_2/RGO composite. Moreover, an excellent rate performance, a good capacitance retention (~70%) and a superior Coulombic efficiency (94−96%) were also observed during the continuous 1300 cycles of galvanostatic charge−discharge.

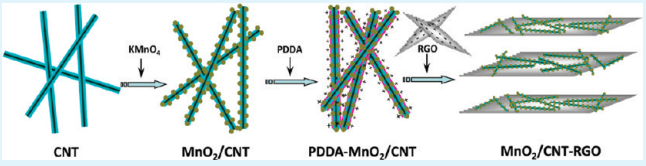

KEYWORDS: *graphene-based composite, carbon nanotubes, MnO_2, supercapacitor electrode*

INTRODUCTION

With the ever-increasing power and energy demand in applications ranging from portable electronics to hybrid electric vehicles and large industrial equipment, great efforts have been devoted in designing and developing the new advanced materials for energy storage. Of the various power source devices, supercapacitors, also known as the ultracapacitors, have received great interest because of their excellent properties such as high power, long cyclic life, and fast charge−discharge rates.[1−3] Carbon materials, metal oxides and conducting polymers have been extensively investigated as electrode materials for supercapacitors application. The carbon materials store energy through charge accumulation at the electrode/electrolyte interfaces. Such character allows very fast energy uptake and delivery, and thus a better power performance. On the other hand, the metal oxides and conductive polymers electrodes store energy through the surface Faradic redox reaction. These pseudocapacitive properties could provide more specific capacitance as compared with the electrical double-layer capacitance (EDLC) of carbon-based electrode materials. However, the pseudocapacitive electrodes involving the Faradic reaction usually suffer from the poor electronic conductivities as well as the limited life cycles.

Graphene, a two-dimensional carbon nanostructure consisiting of single-layer of sp2 carbon atoms, has attracted great scientific and technological intreasts because of its unique preperties such as high therotical surfacea area, excellent elelctronic conductivity, and strong mechanical strength.[4,5] The graphene materials have shown promising application as elelctrode materials in electrochemical energy storage.[6−10] Although chemical reduction of exfoliated graphene oxide (GO) represents a promising pathway for mass production of graphene-based materials,[11−14] the reduced graphene oxide (RGO) layers usually encounters the irreversible agglomeration due to the stong van der Waals interaction between the adjacent layers, leading to substantially reduced surface area of RGO accessible by the elelctrolyte. To overcome this problem, carbon nanotubes (CNTs),[15−19] carbon nanospheres,[20] and carbon black particles[21,22] have been used as the spacer to prevent the adjacent graphene sheets from aggregation. Nevertheless, the specific capacitance of the CNTs/RGO composites remains a low value (120−160 F/g),[17−19] presumably because of the limited surface area accessible by the electrolyte.

However, the specific capacitance of the carbon-based electrode can significantly be enhanced by incorporating the pseudocapacitive components. Among various metals oxides used as supercapacitor electrode, MnO_2 has received great attentions because of its high theoretical pseudocapacitance, low-cost and environmental compatibilities.[23,24] To enhance the specific capacitance of the CNTs/RGO composite, we report herein the synthetic procedure and capacitive behaviors of a hierarchical graphene-based architecture composed of MnO_2-coated CNTs (MnC) and RGO sheets. Our method is based on the electrostatic interaction between RGO sheets and MnC as illustrated in Scheme 1. The MnO_2 nanoflakes grown on CNTs were first achieved by a direct redox reaction between CNTs and aqueous $KMnO_4$. The MnC composite thus obtained was functionalized with poly(diallyldimethylammonium chloride) (PDDA) to endow a positive surface charge. The negatively charged RGO

Received: November 30, 2011
Accepted: January 20, 2012
Published: January 20, 2012

Scheme 1. Schematic Illustration of the Synthetic Procedures for MnC-G Composite

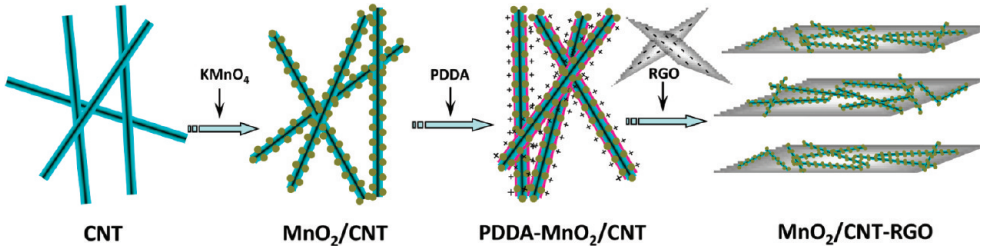

reduced by urea and the positively charged MnC strongly interacts, driving the electrostatic self-assembly between them. The resultant MnC/RGO composite (MnC-G) shows hierarchical nanostructure with MnC uniformly incorporated between graphene sheets. The highly conductive CNTs and the porous nanostructure developed during the self-assembly process provide fast electronic and ionic channels for reversible Faradic redox reaction between MnO_2 nanoflake and aqueous Na_2SO_4 electrolyte, leading to a significantly enhanced capacitive performance as compared with the CNTs/RGO counterpart without MnO_2 incorporated.

EXPERIMENTAL SECTION

Sample Preparation. Commercial multiwalled CNTs with 10−20 nm in diameter and 5−15 μm in length (Shenzhen Nanotech Port Co. Ltd.) were purified by refluxing in diluted HNO_3 (10 wt %) for 12 h. Nanoflakes MnO_2 were grown on the CNTs through a direct redox reaction between CNTs and $KMnO_4$ solution, following a method as described previously.[25,26] Briefly, in a 250 mL flask, 100 mg of CNTs was ultrasonically dispersed in 100 mL of water. Then, 344 mg of $KMnO_4$ was added in the solution. After stirring for 20 min, the solution was heated to 70 °C and refluxed for 3 h under stirring. The precipitates were collected by filtration, rinsed with deionized water and ethanol for several times before drying at 95 °C for 5 h. The functionalization of the MnO_2−CNTs composite (MnC) was achieved by dispersing 150 mg of MnC in 150 mL of water containing 1 mL of PDDA (Typical M_w of 100 000−200 000, 25% aqueous solution, Aldrich). After stirred at room temperature for 5 h, the PDDA-functionalized MnC (PDDA-MnC) was centrifuged, filtrated and rinsed with copious deionized water and ethanol to remove the excessive PDDA. Finally, 30 mg of the dried PDDA-MnC was ultrasonically dispersed in 30 mL of water with pH adjusted to 8.0 using a diluted ammonia solution.

RGO dispersion with a concentration of 0.25 mg/mL was prepared by chemical reduction of grapheme oxide with urea.[7] Afterward, the PDDA-MnC dispersion was added dropwise into the RGO dispersion under vigorous stirring. After being stirred for further 2 h, the black product was filtrated off, rinsed with copious deionized water and ethanol, and finally dried in a vacuum at 80 °C. The as-synthesized sample is denoted as MnC-G*X*, where *X* represents the mass percentage of RGO in the composite (wt %). In a controlled experiment, the CNTs and RGO composite (CNT-G) without MnO_2 incorporated was also prepared through a similar method as described for MnC-G*X*, except that PDDA-CNTs were used as the spacer.

Characterization. The structures of the as-synthesized samples were characterized using X-ray diffraction (XRD) (Bruker AXS D8 Advance Powder X-ray diffractometer) with a CuKa (λ = 1.5418 Å) radiation at a scan rate of 4°/min. The Raman spectra were collected on a WITec CRM200 confocal Raman microscopy system with the excitation line of 488 nm and an air-cooled charge coupled device (CCD) as the detector. Nitrogen adsorption/desorption isotherms were measured at 77 K on Nova 1000. All samples were degassed at 130 °C for 12 h prior to the measurement. The specific surface areas of the samples were calculated using the Brunauer−Emmett−Teller (BET) method with the adsorption data at the relative pressure (P/P_o) range of 0.05−0.2. The morphology of the samples was observed on Zeiss Supra 40VP field-emission scanning electron microscopy (FESEM). High-resolution transmission electron microscopy (HRTEM) images were collected on a field-emission JEOL JEM-2010F at an acceleration voltage of 200 kV. X-ray photoelectron spectroscopy (XPS) spectra were collected on an AXIS Ultra^{DLD} spectrometer (Kratos Analytical Ltd.) using a monochromatized Al Ka X-ray source (1486.71 eV). The Zeta potential profiles of RGO, CNT, and MnC as a function of pH were measured at room temperature on a Malnern Instrument Nano-ZS Zeta potential analyzer. The pH of solution was adjusted using diluted HCl or NaOH solution.

Electrochemical Measurement. The working electrode was prepared by mixing the active material (90 wt %) with carbon black (5 wt %) and polytetrafluoroethylene (5 wt %) in water. The slurry mixture was pasted between two pieces of nickel foam with an area of 1 cm^2 followed by compressed under a pressure of 500 kg/cm^2. The mass loading of each electrode is typically 4.0 mg. The electrochemical behaviors of the electrode materials were investigated using a three-electrode cell, with a Pt foil as a count electrode and an Ag/AgCl electrode as the reference electrodes. The cyclic voltammetry (CV), galvanostatic charge−discharge and electrochemical impedance spectroscopy (EIS) techniques were used to characterize the performances of electrode materials on an Autolab PGSTAT302N electrochemical workstation. A 1.0 mol/L aqueous Na_2SO_4 was used as aqueous electrolyte. The galvanostatic charge−discharge was performed with current densities ranging from 0.1 to 5.0 A/g. The specific capacitance, *C* (F/g), of the electrode material was calculated from the discharge curve according to the following equation[26]

$$C = I\Delta t/(\Delta V m)$$

where *I* is the discharge current (A), Δt is the discharge time (s), ΔV is the voltage change (V) excluding IR drop in the discharge process, and *m* is the mass of the electrode material (g) excluding the binder and conductive carbon black. The electrochemical impedance spectroscopy (EIS) was used to explore the electrochemical behaviors of electrode materials with amplitude of 10 mV in the frequency range of 5 mHz to 100 kHz.

RESULTS AND DISCUSSION

The MnO_2 nanostructure with controlled morphologies grown on various carbonaceous substrates are usually achieved through a redox reaction between carbon and MnO_4^-, following a stoichiometric reaction equation[27]

$$4MnO_4^- + 3C + H_2O \rightarrow 4MnO_2 + CO_3^{2-} + 2HCO_3^-$$

In this work, the CNTs with diameter of 10−20 nm were applied as both reducing agents and substrates for MnO_2 growth. Images a and b in Figure 1 show the morphology of the MnC with different magnifications. The diameter of the individual MnC is increased to 50−60 nm, in sharp contrast to 10−20 nm of the pristine CNTs. It is interesting to note that most of these MnO_2 nanoflakes were vertically grown on the external surface of CNTs (Figure 1b). This morphology differs from previous MnO_2 thin films, which were deposited parallel to the external surface of CNTs.[27] Such hierarchical structure enables more

dx.doi.org/10.1021/am2016848 | ACS Appl. Mater. Interfaces 2012, 4, 1058−1064

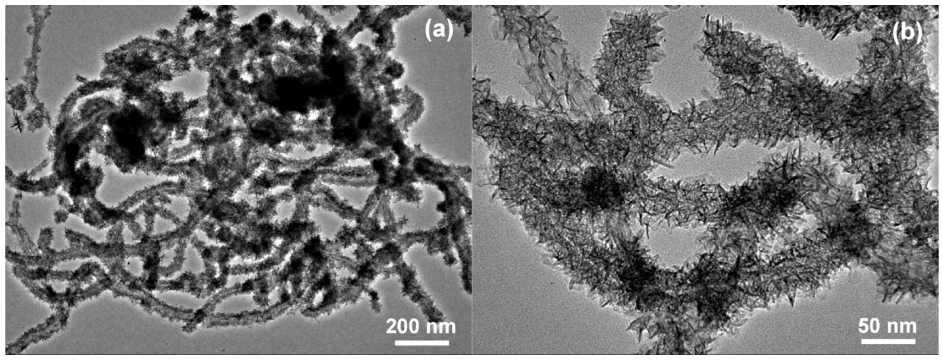

Figure 1. TEM images of MnC with (a) low and (b) high magnifications.

electrochemically active surface area of MnO_2 to be accessed by the electrolyte, promoting the surface redox reaction and EDLC formation. The XRD spectrum of the MnC composite is shown in Figure 2. A strong diffraction peak at 2θ = 25.8° is

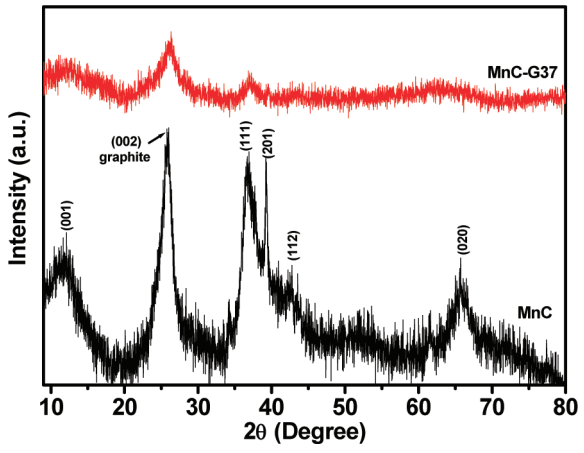

Figure 2. Powder XRD patterns of MnC and MnC-G37 composite.

obviously due to the (002) diffraction of graphite from the CNTs, while the diffraction peaks at 2θ = 11.8, 36.8, 39.3, and 65.7° can be indexed to the (001), (111), (201), and (020) reflections of birnessite-type MnO_2 (JCPDS 42−1317),[28−30] respectively. The energy dispersive spectrum (EDS) of MnC composite clearly shows the presence of Mn, O, K and Cu elements (see Figure S1 in the Supporting Information). The signal of Cu is from the copper grid in TEM measurement, whereas the K element comes from the hydrated K^+ cations in the interlayer of birnessite-type MnO_2.[29] The presence of K^+ in MnC was also confirmed by its XPS spectrum (see Figure S2 in the Supporting Information), where two sharp peaks at 292.7 and 295.5 eV can be clearly observed, corresponding to K $2p_{3/2}$ and K $2p_{1/2}$, respectively. On the basis of the stoichiometric reaction between CNTs and MnO_4^-, a mass content of ~67 wt % MnO_2 was calculated in the MnC composite, consistent with the mass difference before and after redox reaction.

The surface charge of MnC composite was modified by PDDA for the subsequent self-assembly. The PDDA polyelectrolyte is a typical water-soluble quaternary ammonium, which is usually used to functionalize various substrates. Carbonaceous materials such as porous carbon, graphene sheets, and CNTs have been successfully functionalized with PDDA to generate highly positive surface charges.[31−34] The MnC powder after PDDA functionalization was ultrasonically redispersed in water. A homogeneous black dispersion with no evident precipitate was observed even after preparation for 3 days, indicative of significantly improved stability. Figure 3 compares the Zeta potential

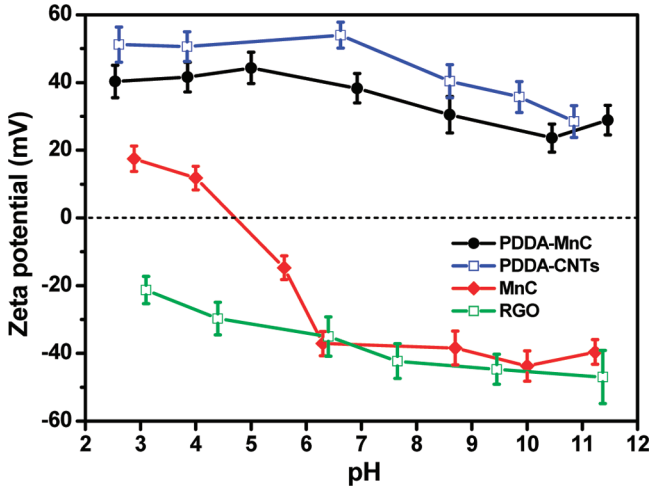

Figure 3. Zeta potential profiles of RGO, CNT, and MnC before and after functionalization with PDDA.

profile of MnC before and after functionalization. It is seen that MnC before functionalization exhibits a negative potential at pH higher than 6, but gradually changes to a positive potential at pH lower than 5. After functionalization with PDDA, a highly positive Zeta potential of ~40 mV was observed in a wide range of pH from 2.5 to 11.5. Such change of surface charge is obviously caused by the adsorption and coverage of PDDA polycation on the external surface of MnC,[35,36] creating a strong electrostatic repulsion between the individual MnC. On the other hand, the RGO suspension reduced by urea exhibits a highly negative potential in the pH range of 3.0−11.5, due to the ionization of the partial oxygen functional groups that were not totally reduced.[7]

At pH of 8.0, the positively charged PDDA-MnC (+34 mV) and the negatively charged RGO (−43 mV) create a strong electrostatic interaction, driving the self-assembly between MnC and RGO. Figure 4 shows the FESEM images of MnC and MnC-G samples with mass contents of RGO varying from 0 to 54 wt %. The pure MnC displays a highly entangled morphology with MnO_2 nanoflakes uniformly coated on the surface of CNTs (Figure 4a), consistent with TEM observation (Figure 1a, b). Figure 4b shows the morphology of the MnC-G20 sample, where the sheetlike RGO and the tubular-like MnC can be clearly identified. Such hierarchical architecture with well-developed porous nanostructure could provide fast

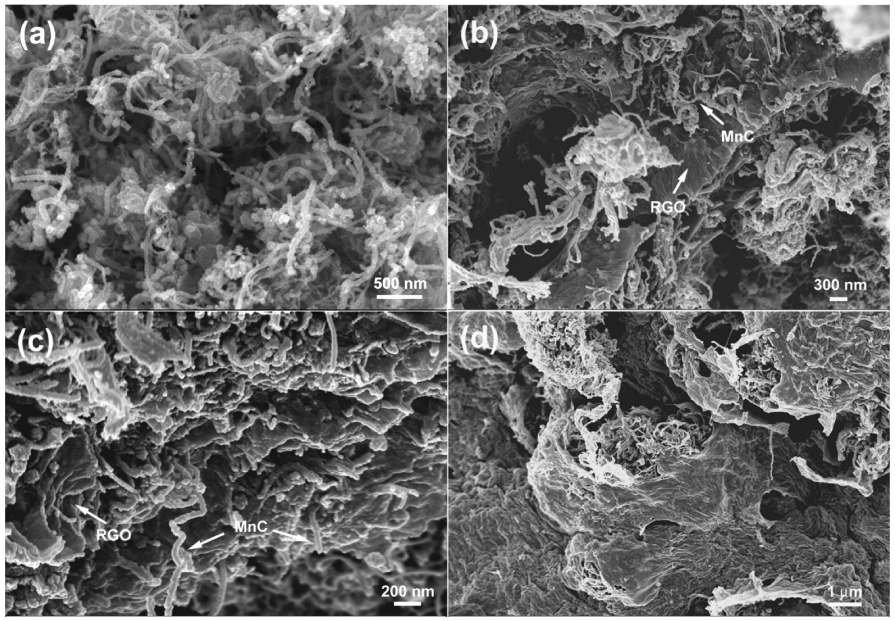

Figure 4. FESEM images of (a) MnC, (b) MnC-G20, (c) MnC-G37, and (d) MnC-G54.

ionic channels for electrochemical energy storage. As the content of RGO increase to 37%, the product shows a structure with MnC uniformly incorporated between the graphene sheets (Figure 4c), forming an interesting sandwiched nanostructure that effectively prevents the RGO sheets from severe agglomeration. As the RGO content increases up to 54 wt %, the MnC-G54 shows the partially aggregated structure (Figure 4d), most likely due to the insufficient MnC that are used as spacer to separate the RGO sheet.

The chemical composition of MnC-G37 sample was investigated by XPS spectroscopy. The strong C, Mn, and O signals in the survey XPS spectra reveal the existence of Mn atoms (see Figure S3 in the Supporting Information). The high-resolution Mn 2p spectra for both MnC and MnC-G37 are presented in Figure 5a. For both samples, two strong peaks at 642 and 653.6 eV can be clearly seen, corresponding to the binding energy of Mn $2p_{3/2}$ and Mn $2p_{1/2}$, respectively.[26,37] The Mn 3s spectra of MnC and MnC-G37 were shown in Figure 5b. The energy separation between the two peaks can be used to determine the manganese valence.[38,39] Energy separation of 4.84 eV indicates Mn^{4+} ions to be dominated in both MnC and MnC-G37 composite. The XPS peaks of O 1s band (Figure 5c) at 529.7 and 531.8 can be assigned to Mn−O−Mn and Mn−O−H in MnC-G37 composite, respectively.[40]

The structures of MnC-G composites were measured by XRD and the representative XRD profile of MnC-G37 is shown in Figure 2. The MnC-G37 exhibits roughly the similar XRD patterns as compared with MnC, except that the weak reflections characteristic of birnessite-type MnO_2 and a broad (002) diffraction of graphite were observed. The local structure of the birnessite-type MnO_2 was analyzed by the Raman spectra (Figure 5d). The sharp and strong G bands at 1582 cm^{-1} and the weak D band at 1358 cm^{-1} evidently come from the CNTs and RGO sheets, respectively, whereas the weak bands at 642 cm^{-1} are related to the symmetric stretching vibration M−O of MnO_6 groups.[41]

The capacitive behavior of MnC-G electrodes was investigated by CV, galvanostatic charge−discharge, and EIS in a three-electrode system with 1.0 mol/L Na_2SO_4 as the aqueous

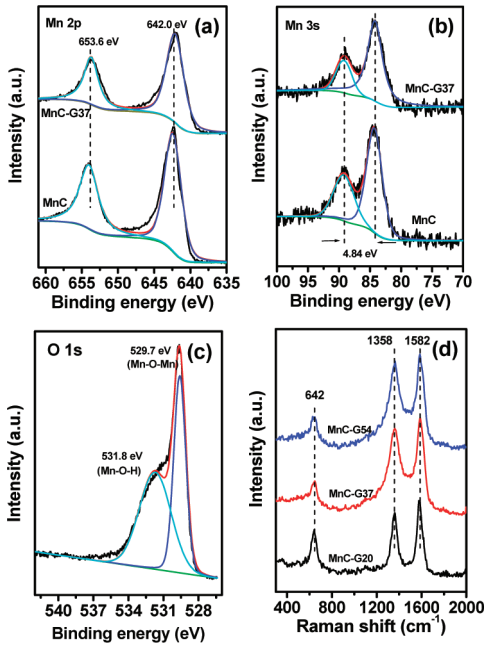

Figure 5. (a) Mn 2p and (b) Mn 3s XPS spectra of MnC and MnC-G37 composite, (c) O 1s spectrum of MnC-G37 and (d) Raman spectra of MnC-G composite.

electrolyte. Figure 6 shows specific capacitances of MnC-G composite measured form galvanostatic discharge curve at constant current density of 0.2 A/g. It is seen that the MnC-G samples exhibit an overall improved specific capacitance as compared with MnC sample. The MnC electrode exhibits a gravimetric capacitance of 145 F/g. In contrast, the MnC-G electrodes show gradually increased specific capacitance with the increase of RGO content and a maximum specific capacitance of 193 F/g was achieved for MnC-G37 sample. This value is slightly higher than 188 F/g of MnO_2 nanosheets deposited on functionalized graphene sheets,[32] 190 F/g of ultrathin MnO_2 nanofibers grown on graphitic carbon spheres,[26] and comparable to 199 F/g of MnO_2 nanoflowers grown on CNTs

dx.doi.org/10.1021/am2016848 | ACS Appl. Mater. Interfaces 2012, 4, 1058−1064

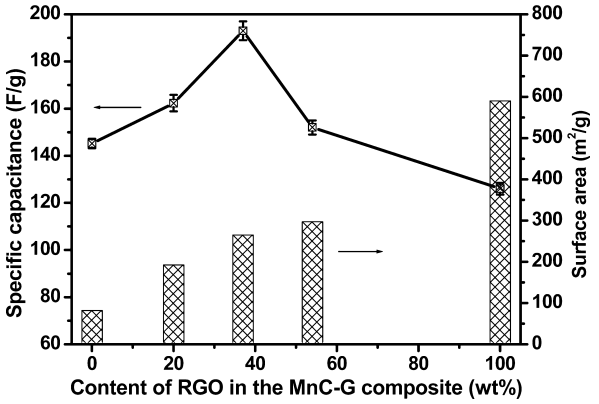

Figure 6. The vVariation of specific capacitance and surface area of graphene-based electrode with the mass percentage of RGO in MnC-G composite.

arrays.[42] Further increase of RGO content to 54 wt % leads to a much reduced specific capacitance of 152 F/g. The pure RGO electrode, however, shows a specific capacitance of 126 F/g in Na_2SO_4 electrolyte, just half of 255 F/g measured in 6.0 mol/L KOH electrolyte.[7] Such comparison supports our previous conclusion that more than 50% capacitance of RGO in KOH electrolyte is contributed from the surface oxygen functional groups. The much reduced specific capacitance of RGO in aqueous Na_2SO_4 reveals a substantial suppression of pseudocapacitance in neutral electrolyte.[43]

The role of these MnO_2 nanoflakes in providing high pseudocapacitance was verified by comparing the CV curves of MnC-G37 and CNT-G. The CNT-G sample without MnO_2 component, was prepared through a similar electrostatic interaction between the positively charged PDDA-CNT and the negatively charged RGO (see Zeta potential in Figure 3). The SEM image in Figures S4 in the Supporting Information reveals that all the CNTs were homogeneously incorporated in the CNT-G composite. In spite of its higher surface area (371 vs 265 m^2/g for MnC-G37), CNT-G exhibits a markedly reduced current response as compared with MnC-G37 (Figure 7a). This electrochemical behavior can be explained by the energy storage mechanism of CNT-G electrode, which relies on physical adsorption of the electrolyte ions on its surface. As a result, a specific capacitance of 69 F/g was measured, almost 3-fold lower than 193 F/g of MnC-G37 electrode, suggesting the significant contribution of MnO_2 nanoflakes in improving the overall performance of MnC-G electrode materials.

The high specific capacitance of MnC-G in comparison with CNT-G is mainly come from Faradic redox between MnO_2 nanoflakes and Na_2SO_4 electrolyte according to the following electrochemical reaction[38,44]

$$MnO_2 + Na^+ + e^- \leftrightarrow MnOONa$$

In contrast, the contribution of double-layer capacitance through surface adsorption of Na^+ by carbon materials is negligible for all MnC-G samples. This is clearly seen by correlating their specific capacitance with their respective surface area (Figure 6). The MnC-G54 and pure RGO electrode, in spite of having large surface area, both exhibit relatively low specific capacitance. On the other hand, the MnO_2/RGO sample, which was prepared by a similar redox reaction between RGO and MnO_4^-, exhibits a much low specific capacitance of 89 F/g, highlighting the synergetic role of RGO, CNTs, and MnO_2 naoflakes in providing a high specific capacitance.

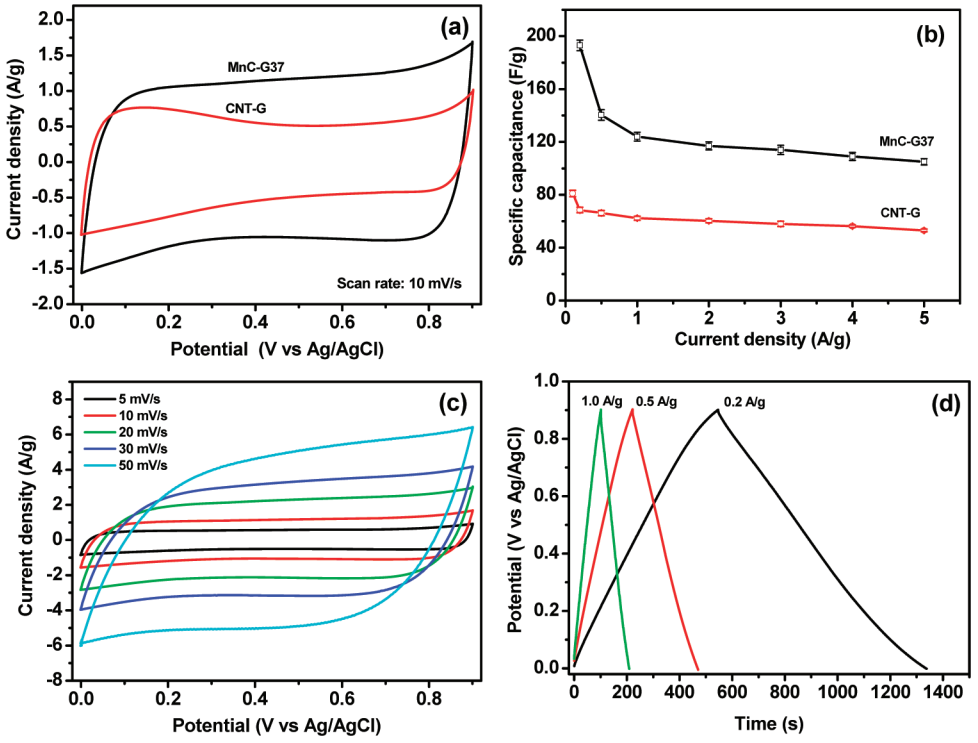

Figure 7. Electrochemical properties of graphene-based electrode measured using a three-electrode system in 1.0 mol/L Na_2SO_4 aqueous electrolyte. (a) CV curves of MnC-37 and CNT-G electrode recorded at a scan rate of 10 mV/s, (b) variation of specific capacitance against current density for MnC-37 and CNT-G electrode, (c) CV curve of MnC-37 electrode at various scan rates, (d) galvanostatic charge−discharge of MnC-37 electrode at current density of 0.2, 0.5, and 1.0 A/g.

dx.doi.org/10.1021/am2016848 | ACS Appl. Mater. Interfaces 2012, 4, 1058−1064

The specific capacitances of MnC-G37 and CNT-G electrode against the current density are plotted in Figure 7b. Both electrodes show gradually decreased capacitance with the increase of the current density. In contrast to CNT-G electrode that stores charges through EDLC, the MnC-G37 electrode shows an evident decrease of specific capacitance as the current density increase from 0.2 to 0.5 A/g, reflecting a much reduced electrochemically active surface area accessed by electrolyte. Nevertheless, the MnC-G37 electrode still remains a specific capacitance of 105 F/g at a current density of 5.0 A/g, much higher than 53 F/g of CNT-G electrode. The excellent capacitive performance of the MnC-G37 electrode was also verified from its CV curves at various scan rates (Figure 7c). It is seen that the current response show corresponding increases with the increase of the scan rate, revealing a good capacitive behavior of MnC-G37 electrode. Moreover, the MnC-G37 electrode still remains a good rectangular CV shape at scan rate as high as 50 mV/s. This superior rate performance is closely related to its unique hierarchical architecture as shown in Figure 4c. The RGO sheets separated by the MnC are capable of offering additional high surface area for double-layer formation, whereas the CNTs backbones in MnC composite are able to provide fast charge propagation. In particular, the MnO_2 nanoflakes coaxially grown on CNTs have more exposed electrochemically active surface area, significantly promoting the reversible Faradic redox reaction between MnO_2 and electrolyte. The galvanostatic charge−discharge curves of MnC-G37 electrode at current density of 0.2, 0.5, and 1.0 A/g were shown in Figure 7d. The nearly symmetric charge−discharge curve reveals a good capacitive behavior and a highly reversible Faradic reaction between Na^+ and MnO_2 nanoflakes.[38,45] At a current density of 1.0 A/g, no obvious IR drop was observed at the beginning of the discharge curve, suggesting a low internal resistance and thus a good rate performance as shown in Figure 7b.

The different charge storage mechanisms of MnC-G37 and CNT-G electrodes are also evident from the impedance analysis (Figure 8). The equivalent circuit diagram used for the fitting of the EIS data is presented in inset of Figure 8, which includes the bulk solution resistance R_s, the charge transfer resistance R_{ct}, a pseudocapacitive element C_p from redox process of MnO_2 and the constant phase element (CPE) to account for the double layer capacitance.[46] It is seen that the CNT-G electrode exhibits an almost vertical line along the imaginary axis in the low-frequency region, which reveals its ideally capacitive behavior due to the non-Faradic charge storage mechanism. The MnC-G37 electrode, however, shows a more inclined curve in the same low-frequency region, suggesting the predominance of pseudocapacitance. In the high-frequency region (inset in Figure 8), both curves intersect the real axis at R_s and $R_s + R_{ct}$, respectively. The bulky solution resistance (R_s) and the charge transfer resistance (R_{ct}) were measured to be 3.4 and 2.4 Ω for CNT-G electrode, respectively. In contrast, the increased R_{ct} (5.4 Ω) of MnC-G37 is resulted from the poor electronic conductivity of MnO_2 (1×10^{-5} to 1×10^{-6} S/cm).[44] Such change of R_{ct} is consistent with the fact that including of insulating components to highly conductive carbon electrode leads to an increased charge transfer resistance.[19,46,47] In the middle-frequency region, the 45° sloped portion known as the Warburg resistance is the consequence of the frequency dependency of ion transport in the electrolyte.[6] The distinct Warburg region for CNT-G electrode suggests a higher ion diffusion resistance. This is most likely

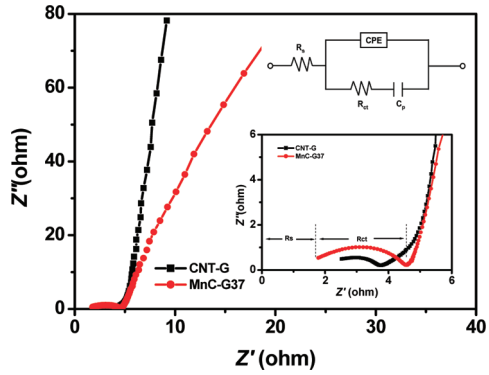

Figure 8. Electrochemical impedance spectra (EIS) of CNT-G and MnC-G37 electrodes with insets showing the high-frequency parts and equivalent circuit diagram used for fitting the EIS data.

related to the smaller diameters of CNTs (10−20 nm) spacers used to separate the RGO sheets. The RGO sheets separated by MnC with the larger diameter (50−60 nm) would create more channels for fast kinetic diffusion of electrolyte ions within the electrode.

The long-term cycling performance of the MnC-G37 electrode in a potential window of 0−0.9 V (vs Ag/AgCl) was measured by the consecutive galvanostatic charge−discharge at current density of 2.0 A/g. The specific capacitance of MnC-G37 electrode was found to gradually decrease from its initial value of 123 to 86 F/g after 1300 continuous cycles (Figure 9).

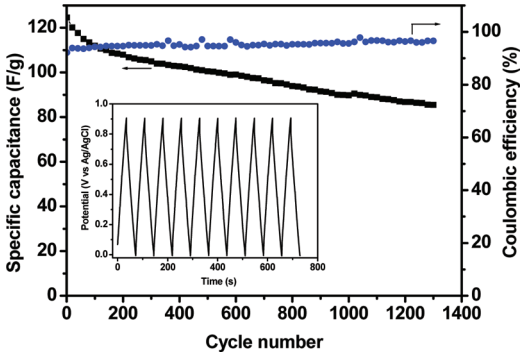

Figure 9. Cycle performance and Coulombic efficiency of MnC-G37 electrode measured at current density of 2.0 A/g. The inset shows the last 10 cycles of galvanostatic charge−discharge.

The poor cycle performance of MnO_2-based electrode is generally affected by two factors: manganese dissolution and oxygen evolution.[44] In our experiment, the applied potential of 0−0.9 V (vs Ag/AgCl) is considered to be a stable electrochemical window, where the oxygen evolution reaction is effectively suppressed. Thus, the poor cyclability of the MnC-G37 electrode may be related to the loss of pseudocapacitive MnO_2. In fact, we found that during the cycling, the electrolyte gradually changed from its initial colorless into yellowish. Such color change is evidently caused by the dissolved manganese oxides from MnC-G37 electrode, resulting in a large capacitance decay of ~30% after 1300 cycles. We believe such severe MnO_2 dissolution may be related to the intercalation/deintercalation of Na^+ into and out of MnO_2 nanostructure during the charge−discharge process. The pseudocapacitive charge storage mechanism together with the continuous volume expansion/contraction of electrode, leads to a mechanically loose connection

dx.doi.org/10.1021/am2016848 | ACS Appl. Mater. Interfaces 2012, 4, 1058−1064

of MnC with the RGO sheets. Nevertheless, the Coulombic efficiency calculated from the ratio between discharge time and charged time remains a quite high value of 94–96% during the whole cycling. The nearly symmetric charge and discharge curves of the last 10 cycles (inset in Figure 9) confirm the highly active and reversible MnO_2 nanoflakes between RGO sheets.

CONCLUSION

A hierarchical architecture consisting of MnC and RGO sheets has been prepared based on the electrostatic self-assembly. The positively charged MnC functionalized with PDDA and negatively charged RGO creates a strong electrostatic interaction, forming a graphene-based nanostructure with MnC uniformly incorporated between RGO sheets. The specific capacitance of MnC-G composite depends on the contents of RGO, and a maximum specific capacitance of 193 F/g was achieved for MnC-G37 electrode at current density of 0.2 A/g, much higher than 69 F/g of the CNT-G and 89 F/g of MnO_2/RGO counterparts. Moreover, the MnC-G37 electrode also shows an excellent rate performance and a superior Coulombic efficiency (94–96%) after 1300 cycles of consecutive galvanostatic charge–discharge. Such excellent performances make the MnC-G hybrid composite the promising electrode for electrochemical energy storage.

ASSOCIATED CONTENT

Supporting Information

EDS and K 2p XPS spectrum of MnC, survey XPS spectra of MnC and MnC-G37 composite, and FESEM image of CNT-G composite. This material is available free of charge via the Internet at http://pubs.acs.org

AUTHOR INFORMATION

Corresponding Author

*Tel: +65-65162236. Fax: +65-67791459. E-mail: luli@nus.edu.sg.

Notes

The authors declare no competing financial interest.

ACKNOWLEDGMENTS

We are grateful for the financial support from the Singapore Ministry of Education under a Tier 2 Grant (Project MOE2008-T2-1-004).

REFERENCES

(1) Miller, J. R.; Simon, P. *Science* **2008**, *321*, 651.
(2) Simon, P.; Gogotsi, Y. *Nat. Mater.* **2008**, *7*, 845.
(3) Liu, C.; Li, F.; Ma, L. P.; Cheng, H. M. *Adv. Mater.* **2010**, *22*, E28.
(4) Geim, A. K.; Novoselov, K. S. *Nat. Mater.* **2007**, *6*, 183.
(5) Ruoff, R. *Nat. Nanotechnol.* **2008**, *3*, 10.
(6) Stoller, M. D.; Park, S.; Zhu, Y.; An, J.; Ruoff, R. S. *Nano Lett.* **2008**, *8*, 3498.
(7) Lei, Z. B.; Lu, L.; Zhao, X. S. *Energy Environ. Sci.* **2012**, DOI: 10.1039/C1EE02478G.
(8) Sun, Y.; Wu, Q.; Shi, G. *Energy Environ. Sci.* **2011**, *4*, 1113.
(9) Liu, C.; Yu, Z.; Neff, D.; Zhamu, A.; Jang, B. Z. *Nano Lett.* **2010**, *10*, 4863.
(10) Biswas, S.; Drzal, L. T. *ACS Appl. Mater. Interfaces* **2010**, *2*, 2293.
(11) Stankovich, S.; Piner, R. D.; Chen, X. Q.; Wu, N. Q.; Nguyen, S. T.; Ruoff, R. S. *J. Mater. Chem.* **2006**, *16*, 155.
(12) Li, D.; Muller, M. B.; Gilje, S.; Kaner, R. B.; Wallace, G. G. *Nat. Nanotechnol.* **2008**, *3*, 101.
(13) Park, S.; Ruoff, R. S. *Nat. Nanotechnol.* **2009**, *4*, 217.
(14) Gao, W.; Alemany, L. B.; Ci, L.; Ajayan, P. M. *Nat. Chem.* **2009**, *1*, 403.
(15) Fan, Z. J.; Yan, J.; Zhi, L. J.; Zhang, Q.; Wei, T.; Feng, J.; Zhang, M. L.; Qian, W. Z.; Wei, F. *Adv. Mater.* **2010**, *22*, 3723.
(16) Zhang, L. L.; Xiong, Z.; Zhao, X. S. *ACS Nano* **2010**, *4*, 7030.
(17) Byon, H. R.; Lee, S. W.; Chen, S.; Hammond, P. T.; Shao-Horn, Y. *Carbon* **2011**, *49*, 457.
(18) Yu, D. S.; Dai, L. M. *J. Phys. Chem. Lett.* **2010**, *1*, 467.
(19) Qiu, L.; Yang, X.; Gou, X.; Yang, W.; Ma, Z.-F.; Wallace, G. G.; Li, D. *Chem.—Eur. J.* **2010**, *16*, 10653.
(20) Lei, Z. B.; Christov, N.; Zhao, X. S. *Energy Environ. Sci.* **2011**, *4*, 1866.
(21) Yan, J.; Wei, T.; Shao, B.; Ma, F.; Fan, Z.; Zhang, M.; Zheng, C.; Shang, Y.; Qian, W.; Wei, F. *Carbon* **2010**, *48*, 1731.
(22) Wang, G.; Sun, X.; Lu, F.; Sun, H.; Yu, M.; Jiang, W.; Liu, C.; Lian, J. *Small* **2012**, *8*, 452.
(23) Wei, W. F.; Cui, X. W.; Chen, W. X.; Ivey, D. G. *Chem. Soc. Rev.* **2011**, *40*, 1697.
(24) Wang, N.; Wu, C.; Li, J.; Dong, G.; Guan, L. *ACS Appl. Mater. Interfaces* **2011**, *3*, 4185.
(25) Ma, S. B.; Ahn, K. Y.; Lee, E. S.; Oh, K. H.; Kim, K. B. *Carbon* **2007**, *45*, 375.
(26) Lei, Z. B.; Zhang, J.; Zhao, X. S. *J. Mater. Chem.* **2012**, *22*, 153.
(27) Jin, X.; Zhou, W.; Zhang, S.; Chen, G. Z. *Small* **2007**, *3*, 1513.
(28) Tang, X.; Li, H.; Liu, Z.-H.; Yang, Z.; Wang, Z. *J. Power Sources* **2011**, *196*, 855.
(29) Kai, K.; Yoshida, Y.; Kageyama, H.; Saito, G.; Ishigaki, T.; Furukawa, Y.; Kawamata, J. *J. Am. Chem. Soc.* **2008**, *130*, 15938.
(30) Xia, H.; Lai, M. O.; Lu, L. *J. Mater. Chem.* **2010**, *20*, 6896.
(31) Wang, S.; Jiang, S. P.; Wang, X. *Nanotechnology* **2008**, *19*, 265601.
(32) Zhang, J. T.; Jiang, J. W.; Zhao, X. S. *J. Phys. Chem. C* **2011**, *115*, 6448.
(33) Zhang, S.; Shao, Y.; Liao, H.; Engelhard, M. H.; Yin, G.; Lin, Y. *ACS Nano* **2011**, *5*, 1785.
(34) Shao, Y. Y.; Zhang, S.; Kou, R.; Wang, X. Q.; Wang, C. M.; Dai, S.; Viswanathan, V.; Liu, J.; Wang, Y.; Lin, Y. H. *J. Power Sources* **2010**, *195*, 1805.
(35) Ni, P.; Li, H. J.; Yang, M. Y.; He, X. X.; Li, Y.; Liu, Z. H. *Carbon* **2010**, *48*, 2100.
(36) Du, X.; Liu, X.; Chen, H.; He, J. *J. Phys. Chem. C* **2009**, *113*, 9063.
(37) Lee, S. W.; Kim, J.; Chen, S.; Hammond, P. T.; Shao-Horn, Y. *ACS Nano* **2010**, *4*, 3889.
(38) Toupin, M.; Brousse, T.; Bélanger, D. *Chem. Mater.* **2004**, *16*, 3184.
(39) Toupin, M.; Brousse, T.; Bélanger, D. *Chem. Mater.* **2002**, *14*, 3946.
(40) Yuan, L.; Lu, X.-H.; Xiao, X.; Zhai, T.; Dai, J.; Zhang, F.; Hu, B.; Wang, X.; Gong, L.; Chen, J.; Hu, C.; Tong, Y.; Zhou, J.; Wang, Z. L. *ACS Nano* **2011**, *6*, 656.
(41) Ma, S. B.; Lee, Y. H.; Ahn, K. Y.; Kim, C. M.; Oh, K. H.; Kim, K. B. *J. Electrochem. Soc.* **2006**, *153*, C27.
(42) Zhang, H.; Cao, G. P.; Wang, Z. Y.; Yang, Y. S.; Shi, Z. J.; Gu, Z. N. *Nano Lett.* **2008**, *8*, 2664.
(43) Lin, Z.; Liu, Y.; Yao, Y.; Hildreth, O. J.; Li, Z.; Moon, K.; Wong, C.-p. *J. Phys. Chem. C* **2011**, *115*, 7120.
(44) Belanger, D; Brousse, T; W. L., J. *Electrochem. Soc. Interface* **2008**, 49.
(45) Qu, Q.; Zhang, P.; Wang, B.; Chen, Y.; Tian, S.; Wu, Y.; Holze, R. *J. Phys. Chem. C* **2009**, *113*, 14020.
(46) Liu, J.; Essner, J.; Li, J. *Chem. Mater.* **2010**, *22*, 5022.
(47) Lei, Z. B.; Chen, Z. W.; Zhao, X. S. *J. Phys. Chem. C* **2010**, *114*, 19867.